A coupled 3D Discrete Elements/Iso-geometric Method for Particle/Structure Interaction Problems

Wei GAO[a,*], Y. T. FENG[b,*]

[a] *School of Electromechanical Engineering, Guangdong University of Technology, Guangzhou, China*
[b] *Zienkiewicz Centre for Computational Engineering, Swansea University, Swansea, UK*

Abstract

To utilize the geometry smoothness of isogeometric analysis (IGA) for solid media and the effectiveness of the discrete element method (DEM) for particulate matters, a coupled three-dimensional (3D) isogeometric/discrete-element method is developed to model the contact interaction between structures and particles. The coupling procedure for handling interactions between isogeometric elements and discrete elements (DEs) includes global search, local search/resolution and interaction force calculation. Since interaction models for contacting particles and isogeometric elements have significant effects on the contact forces in simulations, several commonly used contact models, including liner, Hertz and quadratic models, are investigated. For a small ball impacting a thick plate example, it is found that the Hertz contact model exhibits the best behaviour as the interaction law between a sphere and an isogeometric element in the elastic regime, and no additional correction factor is needed. In addition, an assembly of randomly arranged granular particles impacting a tailor rolled blank is also simulated to further illustrate the applicability of the proposed method.

Keywords: Isogeometric analysis, Discrete element, Coupling, Contact Interaction model

*Corresponding author: Wei GAO, Y. T. FENG
Email addresses: gaowei@gdut.edu.cn; hbweigao@126.com (Wei GAO), y.feng@swansea.ac.uk (Y. T. FENG)

1. Introduction

The discrete element method (DEM) [1] is an effective numerical method to model granular materials (GMs) where the motion of individual particles can be tracked. Due to this feature, DEM has been widely employed in many engineering and industrial applications that exhibit a particulate nature [2]. When DEM is applied to problems where discrete particles are interacting with structures, the structures are usually assumed as rigid without considering their deformation [3], while the interaction between the discrete elements (DEs) and the structures is modeled by contact theories, e.g. the Hertz theory. To account for the effects of the structural deformation on the DE-structure interaction, the finite element method (FEM) can be adopted to analyze the structures. Some coupling FEM/DEM methods are proposed to handle GM-structure interactions [4, 5, 6, 7, 8, 9, 10, 11].

In traditional finite element formulation, the displacement-field of a structure is usually C_0 continuity [12]. Therefore, non-smoothness appears at the common edges and/or nodes of adjacent surfaces in the finite element mesh. However, the particle-structure interaction is sensitive to the interaction surface between the structures and discrete particles. Besides, the non-smoothness of an interaction surface will result in three types of DE/FE contact situations: DE-node, DE-edge and DE-surface contact, which makes the contact algorithm more complicated [9, 10, 13, 14, 15, 16, 17]. In addition, the FE/DE contact force is prone to suffering the so-called time continuity problem, especially when a DE is near FE edges and/or nodes [9, 18, 19], and may also lead to numerical instability due to the generation of superficial energy. A possible solution to this energy instability problem within the coupling DE/FE framework involves using energy conservation based contact theories [5, 20, 21].

The isogeometric analysis (IGA) proposed by Hughes et al. [22] uses the same basis functions as those in CAD [23], e.g. B-spline or NURBS basis functions, to describe the solution field. Consequently, a CAD design model can be used for IGA analysis, and the difference between the CAD design and the IGA model can be minimized. Furthermore, the outer surfaces of an IGA model have the same smoothness as the corresponding CAD model, except at some corners and edges. Because of these advantages over the traditional FEM, a coupled IGA/DEM method has been proposed to model the particle-structure interaction problems [24].

The contact-force calculation has a direct influence on the interaction be-

tween DEs and IGA elements. For linear elastic spheres in DEM, the Hertz contact model is commonly used to calculate the contact force between a pair of contacting elements. In FEM, however, penalty function methods are generally employed to handle the contact constraint and compute the contact force between deformable finite elements. In IGA/DEM contact problems, discrete elements are assumed rigid, while IGA elements are deformable. Hence, it seems not clear at this stage what interaction laws should be employed to compute contact forces between DEs and IGA elements. Therefore, several commonly used contact models, including linear, Hertz and quadratic models, which can be viewed as penalty function based methods in the context of FE contact mechanics, will be investigated to assess their suitability as interaction models for contacting between DEs and IGA elements.

The paper is organized as follows. Section 2 introduces NURBS basis functions and isogeometric approximations. The basic formulations of spherical discrete element models for particulate systems are briefly reviewed in Section 3. Section 4 describes the approach that couples DEs and IGA elements, and focuses on the local contact search/resolution between a sphere and a NURBS surface. Different contact interaction models used for computing contact forces between DEs and IGA elements are assessed in Section 5 for an impact problem, and the best interaction model is identified accordingly. Section 6 presents a numerical example to further demonstrate the applicability of the proposed coupling approach. Conclusions are drawn in Section 7.

2. Isogeometric method

In order to construct a basis function, a knot vector $\boldsymbol{k}^I$ for the I^{th} dimension can be defined as

$$\boldsymbol{k}^I = \left\{ \underbrace{\xi_1^I, \ldots, \xi_{p_I+1}^I}_{(p_I+1)\text{terms}}, \xi_{p_I+2}^I, \ldots, \xi_i^I, \ldots, \xi_{n_I^{\mathrm{k}}}^I, \underbrace{\xi_{n_I^{\mathrm{k}}+1}^I, \ldots, \xi_{m_I^{\mathrm{k}}}^I}_{(p_I+1)\text{terms}} \right\} \tag{1}$$

where ξ_i^I denotes the i^{th} knot. $\boldsymbol{k}^I$ is an ordered sequence of nondecreasing parameter values, i.e. $\xi_i^I \leq \xi_{i+1}^I$, $i = 1, \ldots, n_I^{\mathrm{k}} + p_I$. Here, p_I is the degree of the basis functions, and n_I^{k} denotes the total number of the accompanying control nodes in the I^{th} dimension. $n_I^{\mathrm{e}} = p_I + 1$ is the node number of each control mesh in the I^{th} direction, and $m_I^{\mathrm{k}} = n_I^{\mathrm{k}} + n_I^{\mathrm{e}}$ denotes the value numbers of the knot vector $\boldsymbol{k}^I$. The parameter space for a 3D IGA element (i, j, k) can be defined as the non-zero knot spans $[\xi_i^1, \xi_{i+1}^1)$, $[\xi_j^2, \xi_{j+1}^2)$ and $[\xi_k^3, \xi_{k+1}^3)$.

2.1. B-spline basis functions

Given a knot vector $\boldsymbol{k}^I$, the B-spline basis function $\phi_{i,p_I}(\xi^I)$, can be defined recursively by the Cox-de-Boor formula [25, 26] as

$$\phi_{i,p_I}(\xi^I) = \frac{\xi^I - \xi_i^I}{\xi_{i+p_I}^I - \xi_i^I}\phi_{i,p_I-1}(\xi^I) + \frac{\xi_{i+p_I+1}^I - \xi^I}{\xi_{i+p_I+1}^I - \xi_{i+1}^I}\phi_{i+1,p_I-1}(\xi^I), \text{ for } p_I \geq 1 \quad (2)$$

with the zeroth degree basis function defined as

$$\phi_{i,0}(\xi^I) = \begin{cases} 1, & \text{if } \xi_i^I \leq \xi^I < \xi_{i+1}^I \\ 0, & \text{otherwise} \end{cases} \quad (3)$$

When evaluating a basis function, some repeating knots may result in a quotient of form $\square/0$ which is defined as zero. The non-negative $\phi_{i,p_I}(\xi^I)$ is simplified as $\phi_i(\xi^I)$ below for conciseness. $\phi_i(\xi^I)$ is infinitely differentiable in the interior of any non-zero knot span (ξ_i^I, ξ_{i+1}^I), but is $(p_I - k_I)$ times continuously differentiable at a knot ξ_i^I where k_I is the knot multiplicity. In any given knot span $[\xi_i^I, \xi_{i+1}^I)$, among all the basis shape functions $\phi_i(\xi^I)$, there are at most p_I+1 nonzero functions

$$\begin{cases} \phi_m(\xi^I) \neq 0, \text{ for } m = (i - p_I), \ldots, i \\ \phi_m(\xi^I) = 0, \text{ for } m < (i - p_I) \text{ or } m > i \end{cases} \quad (4)$$

2.2. NURBS basis functions, surface and element

A NURBS basis function $R_i(\xi^I)$ is defined from B-spline basis functions as

$$R_i(\xi^I) = \frac{\phi_i(\xi^I)\omega_i}{\sum_{m=0}^{n_I^{\mathrm{k}}} \phi_m(\xi^I)\omega_m} \quad (5)$$

where $\omega_i > 0$ is the i^{th} weight. Combining with Eq. (4), $R_i(\xi^I)$ in the knot span $[\xi_i^I, \xi_{i+1}^I)$ can be represented as

$$R_i(\xi^I) = \frac{\phi_i(\xi^I)\omega_i}{\sum_{m=i-p_I}^{i} \phi_m(\xi^I)\omega_m} \quad (6)$$

In this knot span, only $p_I + 1$ basis functions may be greater than zero, i.e.

$$R_{i-p_I}(\xi^I), \ldots, R_i(\xi^I) \geq 0, \text{ for knot span } [\xi_i^I, \xi_{i+1}^I) \quad (7)$$

By linearly combining the NURBS basis functions with the control nodes, an arbitrary point in or on a NURBS geometry can be determined. For instance, a NURBS curve, $\boldsymbol{C}_i(\xi^1)$, can be constructed by

$$\boldsymbol{C}_i(\xi^1) = \sum_{m=m_0}^{i} R_m(\xi^1)\boldsymbol{x}_m \tag{8}$$

where $\boldsymbol{x}_m$ is the position vector of the control node m. To illustrate this construction, a two-dimensional (2D) second-degree NURBS curve is displayed in Fig. 1, where N_i is the i^{th} control node and C_i denotes the i^{th} section of this NURBS curve. The basis functions, parameter space, curve sections and control nodes are depicted in Table 1.

It can be seen from Fig. 1 and Table 1 that for IGA, control meshes generally do not coincide with the constructed geometry (curve, surface or volume), and control nodes may locate outside or inside the geometry constructed from the control mesh. However, for FEM, element nodes are always on its constructed geometry. This difference between FEM and IGA is mainly caused by different natures of their basis functions. The basis functions of FEM are usually interpolatory, while the basis functions of IGA, e.g. B-spline and NURBS, are usually not.

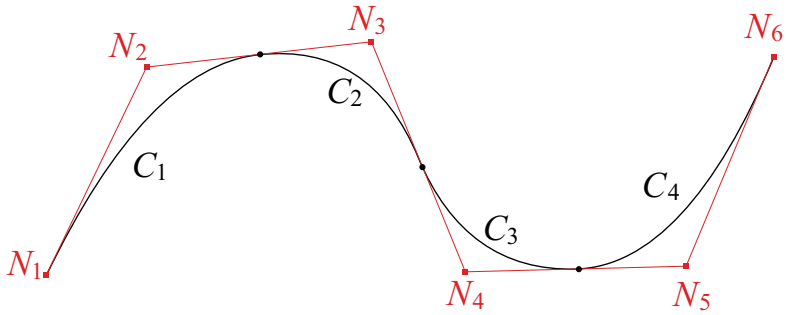

Figure 1: An opened second-degree NURBS curve with the knot vector $\boldsymbol{k}^I = \{\xi_1^1, \xi_2^1, \xi_3^1, \xi_4^1, \xi_5^1, \xi_6^1, \xi_7^1, \xi_8^1, \xi_9^1\}$, with repetitive knots at the two ends $\xi_1^1 = \xi_2^1 = \xi_3^1$, $\xi_7^1 = \xi_8^1 = \xi_9^1$

In three dimensions, an arbitrary point in a NBRBS volume can also be determined from the control nodes as

$$\boldsymbol{V}_{ijk}(\xi^1, \xi^2, \xi^3) = \sum_{m=m_0}^{i} \sum_{n=n_0}^{j} \sum_{l=l_0}^{k} R_{mnl}(\xi^1, \xi^2, \xi^3)\boldsymbol{x}_{mnl} \tag{9}$$

Table 1: The basis functions, parameter space, curve sections and control nodes

	Curve C_1	Curve C_2	Curve C_3	Curve C_4
Control node	N_1, N_2, N_3	N_2, N_3, N_4	N_3, N_4, N_5	N_4, N_5, N_6
Basis function	R_1, R_2, R_3	R_2, R_3, R_4	R_3, R_4, R_5	R_4, R_5, R_6
Parameter space	$[\xi_3^1, \xi_4^1)$	$[\xi_4^1, \xi_5^1)$	$[\xi_5^1, \xi_6^1)$	$[\xi_6^1, \xi_7^1)$

where $m_0 = i - p_1$, $n_0 = j - p_2$, $l_0 = k - p_3$; $\boldsymbol{x}_{ijk}$ denotes the position vectors at the control nodes; and R_{ijk} can be rewritten as

$$R_{ijk}(\xi^1, \xi^2, \xi^3) = \frac{\phi_i(\xi^1)\phi_j(\xi^2)\phi_k(\xi^3)\omega_{ijk}}{\sum_{m=m_0}^{i}\sum_{n=n_0}^{j}\sum_{l=l_0}^{k}\phi_m(\xi^1)\phi_n(\xi^2)\phi_l(\xi^3)\omega_{mnl}}. \tag{10}$$

By inheriting the geometric parameters from the NURBS volume, and then setting $\xi^3 = 0$ or 1, a NURBS surface patch can be fully obtained [27]. For instance, the (lower) surface of the NURBS element (i, j, k) $\boldsymbol{S}_{ij}(\xi^1, \xi^2)$ can be determined by setting $\xi^3 = 0$ and substituting Eq. (10) into Eq. (9) as

$$\boldsymbol{S}_{ij}(\xi^1, \xi^2) = \sum_{m=m_0}^{i}\sum_{n=n_0}^{j} R_{mn}(\xi^1, \xi^2)\boldsymbol{x}_{mn} \tag{11}$$

where $\boldsymbol{x}_{mn}$ denote the position vectors at the control nodes for the surface $\xi^3 = 0$ and

$$R_{mn}(\xi^1, \xi^2) = \frac{\phi_m(\xi^1)\phi_n(\xi^2)\omega_{mn}}{\sum_{M=m_0}^{i}\sum_{N=n_0}^{j}\phi_M(\xi^1)\phi_N(\xi^2)\omega_{MN}} \tag{12}$$

is the NURBS surface shape function associated with the control node (m, n). Here, m denotes the m^{th} node in the ξ^1 direction, while n denotes the n^{th} one in the ξ^2 direction; and ω_{mn} is the weighting factor of the control node (m, n) for the surface $\xi^3 = 0$. In order to evaluate the projection of a point on the NURBS surface (see Section 4.2), the derivatives of the NURBS surface with $\xi^3 = 0$ can be calculated as

$$\frac{\partial \boldsymbol{S}_{ij}(\xi^1, \xi^2)}{\partial \xi_I} = \sum_{m=m_0}^{i}\sum_{n=n_0}^{j}\frac{\partial R_{mn}(\xi^1, \xi^2)}{\partial \xi_I}\boldsymbol{x}_{mn} \quad (I = 1, 2) \tag{13}$$

where

$$\frac{\partial R_{mn}(\xi^1,\xi^2)}{\partial \xi_I} = \frac{\omega_{mn}}{\omega}\Big\{\frac{\partial[\phi_m(\xi^1)\phi_n(\xi^2)]}{\partial \xi^I} - R_{mn}(\xi^1,\xi^2)\frac{\partial \omega}{\partial \xi^I}\Big\} \tag{14}$$

with

$$\omega = \sum_{m=m_0}^{i}\sum_{n=n_0}^{j}\phi_m(\xi^1)\phi_n(\xi^2)\omega_{mn} \tag{15}$$

2.3. The governing equations for IGA element

The governing equations for an IGA element can be represented as

$$\boldsymbol{M}_{\mathrm{e}}\ddot{\boldsymbol{u}}_{\mathrm{e}} = \boldsymbol{f}_{\mathrm{e}}^{\mathrm{ext}} - \boldsymbol{f}_{\mathrm{e}}^{\mathrm{int}} \tag{16}$$

where $\boldsymbol{u}_{\mathrm{e}}$ denotes the nodal displacement vector of the control mesh; $\ddot{\boldsymbol{u}}_{\mathrm{e}}$ denotes the nodal acceleration vector; $\boldsymbol{f}_{\mathrm{e}}^{\mathrm{ext}}$ is the external nodal force vector; and $\boldsymbol{f}_{\mathrm{e}}^{\mathrm{int}}$ is the internal nodal force vector calculated by

$$\boldsymbol{f}_{\mathrm{e}}^{\mathrm{int}} = \int_{V_e}\boldsymbol{B}^{\mathrm{T}}\boldsymbol{\sigma}\mathrm{d}V \tag{17}$$

where $\boldsymbol{\sigma} = [\sigma_{11}, \sigma_{22}, \sigma_{33}, \sigma_{23}, \sigma_{13}, \sigma_{12}]$ is the Voigt notation description of the stress tensor. For an IGA element (i, j, k), the strain matrix $\boldsymbol{B}$ can be represented as

$$\boldsymbol{B} = [\boldsymbol{B}_{m_0n_0l_0}, \ldots, \boldsymbol{B}_{mnl}, \ldots, \boldsymbol{B}_{ijk}] \tag{18}$$

in which $m_0 = i - p_1$, $n_0 = j - p_2$, $l_0 = k - p_3$; and $\boldsymbol{B}_{mnl}$ can be expressed as

$$\boldsymbol{B}_{mnl} = \begin{bmatrix} \frac{\partial R_{mnl}}{\partial x_1} & 0 & 0 & 0 & \frac{\partial R_{mnl}}{\partial x_3} & \frac{\partial R_{mnl}}{\partial x_2} \\ 0 & \frac{\partial R_{mnl}}{\partial x_2} & 0 & \frac{\partial R_{mnl}}{\partial x_3} & 0 & \frac{\partial R_{mnl}}{\partial x_1} \\ 0 & 0 & \frac{\partial R_{mnl}}{\partial x_3} & \frac{\partial R_{mnl}}{\partial x_2} & \frac{\partial R_{mnl}}{\partial x_1} & 0 \end{bmatrix}^{\mathrm{T}} \tag{19}$$

3. Contact model for spherical elements

Various contact models can be employed to handle the interaction of granular materials for a wide range of applications [28, 29]. In the present work, only spherical discrete elements are considered and no friction force will be taken into account.

When two spheres i and j are in contact, as shown in Fig. 2, the contact model based on the Hertz-Mindlin theory is used to calculate the contact

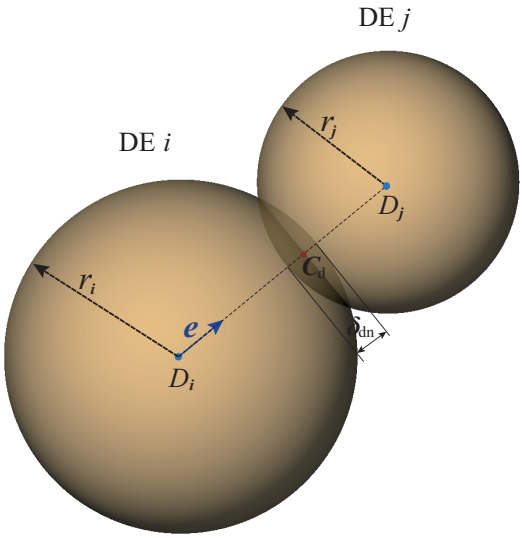

Figure 2: Two discrete elements in contact

force. The contact force in this model is usually divided into normal and tangential contact components. The normal contact force $\boldsymbol{f}_{\text{dn}}$ for the element i can be calculated based on the Hertz model [30] as

$$\boldsymbol{f}_{\text{dn}} = \frac{4}{3} E^* (r^* \|\boldsymbol{\delta}_{\text{dn}}\|^{1/2}) \boldsymbol{\delta}_{\text{dn}} \tag{20}$$

where $\boldsymbol{\delta}_{\text{dn}}$ is the overlap vector determined by

$$\boldsymbol{\delta}_{\text{dn}} = (r_i + r_j - \|\boldsymbol{d}_i - \boldsymbol{d}_j\|)\boldsymbol{e} \tag{21}$$

in which $\boldsymbol{e} = (\boldsymbol{d}_i - \boldsymbol{d}_j)/(\|\boldsymbol{d}_i - \boldsymbol{d}_j\|)$ is a unit vector passing through the DE centroids; and r_i and r_j are the radii of DEs i and j respectively. The equivalent radius r^* and Young's modulus E^* are defined as

$$r^* = \frac{r_i r_j}{r_i + r_j}, \tag{22}$$

$$E^* = \frac{E_i E_j}{(1-\nu_i^2)E_j + (1-\nu_j^2)E_i} \tag{23}$$

where E_i and E_j are the Young's moduli of the two DEs, and ν_i and ν_j denote their Poisson's ratios.

The tangential contact force $\boldsymbol{f}_{\mathrm{ds}}$ for the element i can be determined based on the Mindlin theory as

$$\boldsymbol{f}_{\mathrm{ds}} = \frac{16}{3} G^{*} (r^{*} |\boldsymbol{\delta}_{\mathrm{dn}}|)^{1/2} \boldsymbol{\delta}_{\mathrm{ds}}. \tag{24}$$

where G^{*} and $\boldsymbol{\delta}_{\mathrm{ds}}$ are, respectively, the equivalent shear modulus and tangential relative displace and are defined as

$$G^{*} = \frac{G_i G_j}{(2-\nu_i) G_j + (2-\nu_j) G_i}, \tag{25}$$

$$\boldsymbol{\delta}_{\mathrm{ds}} = \int_{t_1}^{t_2} \boldsymbol{v}_{\mathrm{s}}' \mathrm{d}t \tag{26}$$

where G_i and G_j are the shear moduli of the two DEs; $\boldsymbol{v}_{\mathrm{s}}'$ is the relative velocity at the contact point C_{d}; and $[t_1, t_2]$ is the contact time interval.

4. Coupling approach

The coupling between IGA elements and discrete elements are divided into three stages: global search, local search/resolution and contact force computation.

4.1. Global search

The global search aims to detect potential contact pairs between IGA elements (or NURBS surfaces) and discrete elements based on their axis aligned bounding box (AABB) representations. This step crucially depends on the strong convex hull property of NURBS surfaces which states that *a NURBS surface is fully enclosed in the convex hull of its control nodes*. Therefore, the bounding box of a NURBS surface can be obtained as the bounding box of its control points. Hence, by detecting the overlap between the bounding boxes of DEs and the convex hulls of NURBS surfaces, the potential contact pairs between DEs and NURBS surfaces can be attained. To illustrate this clearly, a two-dimensional (2D) case is shown in Fig. 3, where H_2 denotes the convex hull of IGA element 2. When the DE bounding box overlaps with that of H_2, the DE and IGA element 2 constitute a candidate contact pair.

To handle the contact problem involving a large number of DEs and IGA surfaces, the CGRID method [21, 31] is extended to detect bounding boxes that are in overlap. This detection process is often time-consuming so it is

desirable to perform the detection only when necessary rather than at every time step. To achieve this, the bounding boxes of both DE radii and NURBS surfaces are extended by (small) buffer zones (see Fig. 3).

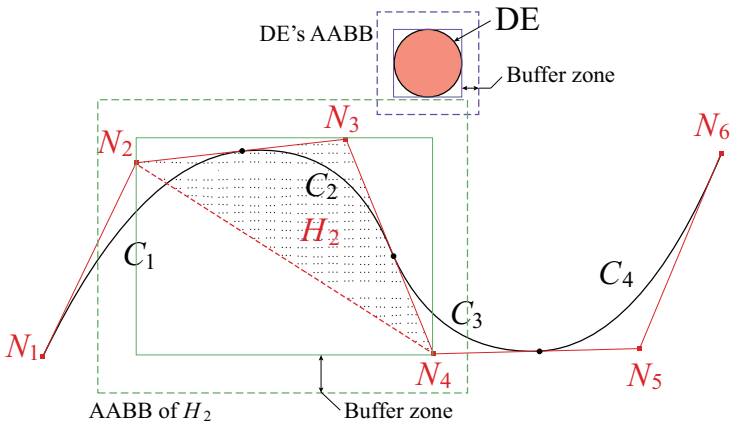

Figure 3: Bounding boxes of a DE and a NURBS element - the convex hull contains the corresponding second-degree NURBS curve (degree $p_1 = 2$, node number of a control polygon $n_1^e = p_1 + 1 = 3$)

4.2. Local search/resolution

Based on potential candidate contact pairs between DEs and NURBS surfaces obtained in the previous global search stage, the actual contact state between a contact pair will be resolved in the local resolution stage based on their true geometric shapes. When the pair is in overlap, their contact feature, including contact position, penetrations and normal direction, will be determined.

In isogeometric analysis, commonly used local contact methods mainly fall into three groups, the Mortar method [32, 33, 34], the Gauss-point-to-surface (GPTS) method [27, 35, 36] and the node-to-surface (NTS) method [37]. Because of the particulate nature of GMs, the NTS method is adopted for the local search/resolution for an IGA/DEM contact pair.

Fig. 4 shows a possible contact scenario between a sphere (DE) and a NURBS surface. In this figure, D is the center of the DE, C denotes the closest projection of D onto the NURBS surface, and $\boldsymbol{x}$ and $\boldsymbol{d}$ denote the position vectors of C and D, respectively. The DE center, D, is treated as the slave node in the NTS method.

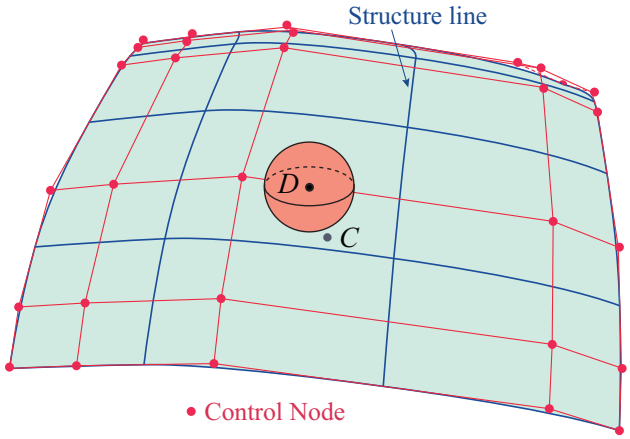

Figure 4: The closest projection of a DE center on a NURBS surface

The closest projection C, i.e. $\boldsymbol{x}(\xi_{\mathrm{c}}^1, \xi_{\mathrm{c}}^2)$, is determined by solving the following equations simultaneously

$$\frac{\partial \boldsymbol{x}}{\partial \xi^1}|_{(\xi_{\mathrm{c}}^1, \xi_{\mathrm{c}}^2)} \cdot [\boldsymbol{d} - \boldsymbol{x}(\xi_{\mathrm{c}}^1, \xi_{\mathrm{c}}^2)] = 0 \tag{27}$$

$$\frac{\partial \boldsymbol{x}}{\partial \xi^2}|_{(\xi_{\mathrm{c}}^1, \xi_{\mathrm{c}}^2)} \cdot [\boldsymbol{d} - \boldsymbol{x}(\xi_{\mathrm{c}}^1, \xi_{\mathrm{c}}^2)] = 0 \tag{28}$$

where ξ_{c}^1 and ξ_{c}^2 are the unknown parameter coordinates at the projection on the NURBS surface.

The Brent iteration method [38, 39] is adopted to solve Eqs. (27) and (28) simultaneously. Because of its local convergence nature, the initial values of the parameter coordinates, ξ_{c}^1 and ξ_{c}^2, need to be estimated by a robust method. Because only the squared distance function $s_{\mathrm{d}} = \|\boldsymbol{d} - \boldsymbol{x}(\xi_{\mathrm{c}}^1, \xi_{\mathrm{c}}^2)\|^2$ is needed, rather than its derivatives [40, 41], the simplex method is considered to be a robust optimization method, and thus is employed for the initial value estimation of the Brent iteration. Refer to [24] for more detail on how to solve Eqs. (27) and (28).

Once the parameter coordinates ξ_{c}^1 and ξ_{c}^2 are determined, the projection $\boldsymbol{x}_{\mathrm{c}} = \boldsymbol{x}(\xi_{\mathrm{c}}^1, \xi_{\mathrm{c}}^2)$ on the closest NURBS patch (i, j) can be computed as

$$\boldsymbol{x}_{\mathrm{c}} = \sum_{m=m_0}^{i} \sum_{n=n_0}^{j} R_{mn}(\xi_c^1, \xi_c^2) \boldsymbol{x}_{mn};\ m_0 = i - p_1; n_0 = j - p_2 \tag{29}$$

where m and n denote, respectively, the m^{th} and n^{th} control nodes of the surface patch in both ξ^1 and ξ^2 directions; $R_{mn}(\xi_c^1, \xi_c^2)$ is the shape-function value at the projection; and $\boldsymbol{x}_{mn}$ denotes the position vector of the control node.

In comparison with the DE radius, the penetration between a DE and a NURBS surface is generally small. Hence, the DE centroid is always assumed to locate outside the NURBS volume of IGA elements. The relative position of a DE and a NURBS surface can be characterized by the penetration vector $\boldsymbol{\delta}$

$$\boldsymbol{\delta} = \begin{cases} (r - |\boldsymbol{x}_d - \boldsymbol{x}_c|)\boldsymbol{n}, & r - |\boldsymbol{x}_d - \boldsymbol{x}_c| > 0 \\ \boldsymbol{0}, & \text{otherwise} \end{cases} \tag{30}$$

where r denotes the DE radius, and $\boldsymbol{n} = (\boldsymbol{x}_d - \boldsymbol{x}_c)/\|\boldsymbol{x}_d - \boldsymbol{x}_c\|$ is the unit normal vector at the projection.

The central difference method, as an explicit scheme, is adopted for the subsequent time integration of the whole system. Since its critical time step is usually very small, the projection may in general shift slightly on the NURBS surface in consecutive time steps. Hence, it is advisable to assign the initial parameter values of the Brent method in the current time step from the converged value in the last time step. By employing this initial estimation, the Brent method usually converges in five iterations or less. Consequently, the simplex iteration is unnecessary to be preformed at every time step.

4.3. Contact force computation

After the projection of a DE centroid on a NURBS surface and the penetration vector have been computed in the local search/resolution stage, the contact force between the DE and the IGA element can be calculated. In discrete element methods, the deformation of discrete elements is equivalent to their overlaps, while the discrete element geometries remain unchanged. The contact force between discrete elements are calculated based on an appropriate contact interaction law. The Hertz contact model is accurate for linear elastic spheres with a (relatively) small impact velocity.

In contrast, in the FEM or IGA contact problem, elements are generally deformable, and the contact interaction between contacting elements is handled by using a penalty based method, which essentially aims to approximately enforce the impenetration condition. However, the contact interaction between a (nominally) rigid discrete element and a deformable isogeometric element does not fall in either of the above categories. Hence, it is not appar-

ent what interaction model should be adopted to compute the contact forces between a DE sphere and an IGA element.

To address this important issue, some commonly used contact models including the linear, Hertz and quadratic models, which could also be viewed as penalty based models, are employed to calculate the contact forces:

$$\text{Linear:} \qquad \boldsymbol{f}_{\mathrm{L}} = \frac{4}{3}\lambda E^{*}(r^{*})^{1/2}\boldsymbol{\delta} \tag{31}$$

$$\text{Hertz:} \qquad \boldsymbol{f}_{\mathrm{H}} = \frac{4}{3}\lambda E^{*}(r^{*}\|\boldsymbol{\delta}\|)^{1/2}\boldsymbol{\delta} \tag{32}$$

$$\text{Quadratic:} \qquad \boldsymbol{f}_{\mathrm{S}} = \frac{4}{3}\lambda E^{*}(r^{*})^{1/2}\|\boldsymbol{\delta}\|\boldsymbol{\delta} \tag{33}$$

where the equivalent Young's modulus E^{*} is calculated from the material properties of the surface and the DE; r^{*} is the equivalent radius; and λ is a corrective constant, termed the penalty factor. As the curvature radius of the NURBS surface at the contact point is usually much larger than the DE radius, thus from Eq. (22) the equivalent r^{*} can be approximated to be the DE radius r.

The assessment of the accuracy of these contact interaction models for an impact problem will be performed in the next section.

Because the penetration vector $\boldsymbol{\delta}$ points to the DE centroid, the contact force $\boldsymbol{f}$ acts through the DE centroid without generating a torque. The reciprocal reaction force acting on the IGA element can be distributed to the corresponding control nodes by using the nodal shape functions. Because only the control nodes of the contact surface have nonzero shape-function values, the contact force should only be distributed to these control nodes, and the corresponding distributed contact forces $\boldsymbol{f}_{mn}$ are given by

$$\boldsymbol{f}_{mn} = -R_{mn}(\xi_{\mathrm{c}}^{1}, \xi_{\mathrm{c}}^{2})\boldsymbol{f} \tag{34}$$

where $R_{mn}(\xi_{\mathrm{c}}^{1}, \xi_{\mathrm{c}}^{2})$ is the shape-function value at the contact point for the control node at the m^{th} and n^{th} positions along the ξ^{1} and ξ^{2} directions respectively.

Because of the C^{0} continuity nature of a FE mesh surface, a DE/FE contact method may have to deal with several distinct contact cases: DE-surface, DE-edge and/or DE-node contact [9, 16, 10, 42], and thus may lead to the time discontinuity of the contact force. The IGA/DEM method proposed here, however, only needs to handle the the contact problem between DEs

and smooth NURBS surfaces. As a result, the computed contact forces are always time-continuous, if ignoring contacts between DEs and sharp corners or C^0 edges of a NURBS patch or patches.

5. Assessment of contact interaction models for coupled IGA/DEM

In this section, the accuracy of the contact models listed in Eqs. (31), (32) and (33) will be assessed by a benchmark problem where a small linear elastic ball impacts with a thick elastic plate.

This problem has long been investigated. Its analytical solution has been derived based on the Hertzian impact theory and elastic wave propagation, and has also been verified by experiments. The impact force history is very well approximated by a function of half sine as [43, 44]

$$f(t) = \begin{cases} f_{\max}\sin(\pi t/t_{\rm c})^{3/2},\ 0 \le t < t_{\rm c} \\ 0,\ t \ge t_{\rm c} \end{cases} \tag{35}$$

where the maximum force $f_{\max}$ is

$$f_{\max} = 1.917\rho_{\rm b}^{3/5} r_{\rm b}^2 (\pi E^*)^{2/5} V_0^{6/5}; \tag{36}$$

while the duration of the contact interaction $t_{\rm c}$ is determined as

$$t_{\rm c} = 4.53 r_{\rm b} \left(\frac{4\rho_{\rm b}}{3E^*}\right)^{2/5} V_0^{-1/5} \tag{37}$$

In Eqs. (36-37), E^* is the equivalent Young's modulus calculated from the two contact bodies; $\rho_{\rm b}$ $r_{\rm b}$ and V_0 are the density, radius and initial velocity of the ball respectively.

The square plate is assumed homogeneous, and is fully fixed on its four sides. The dimensions, material properties, initial conditions of the impact system are depicted in Table 2. Initially, the ball with the velocity of 1.0 m/s is impacting with the center of the top-surface of the plate.

In the simulation, the plate is analyzed using IGA, while the ball is modeled by one spherical discrete element, as shown in Fig. 5. The IGA region is divided into $31 \times 31 \times 8 = 7688$ IGA elements of degree two with the same knot span in each direction. The interaction between the DE and the IGA region is dealt with by the IGA/DEM coupling approach proposed. For each IGA element, the Gaussian integration is employed with three points

Table 2: The geometry, material properties and initial conditions of the impact system

	Density (kg/m^3)	Young's modulus	Poisson's ratio ν	Radius or width	Thickness	Initial velocity
Ball	2480	74.6 GPa	0.2285	1.0 mm	-	1.0 m/s
Plate	7850	210.6 GPa	0.2860	610 mm	50.1 mm	0.0 m/s

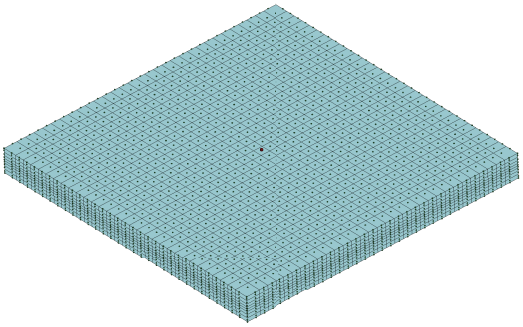

Figure 5: IGA/DEM model of small impacting massive plate

in each direction of the parameter space. The time step is chosen to be 10^{-5} ms, which is much smaller than the corresponding critical time steps of the central difference method.

Because the penalty factor λ in each contact model to be evaluated has a direct influence on computational results, different values of the penalty factor will also be chosen to observe its influence on the results.

5.1. Hertz contact model

The Hertz contact model is first considered. The time histories of the contact force with different penalty factors $\lambda = 0.6, 0.8, 1.0$ and 1.2 are compared with the analytical solution and displayed in Fig. 6. In this figure, the contact-force history with the penalty factor λ= 1.0 is almost identical to the analytical one. Besides, the curve of the contact force with a larger penalty factor tends to reach a higher peak value in a shorter time, as expected.

The impact ball with different Young's moduli and Poisson's ratios are also considered, but the other parameters and conditions are kept unchanged as shown in Table 2. The contact-force histories of the impact ball with Young's moduli E = 50, 74.6, 100, 200 and 300 GPa and the penalty factor $\lambda = 1.0$ are compared with the analytical solutions and displayed in Fig. 7.

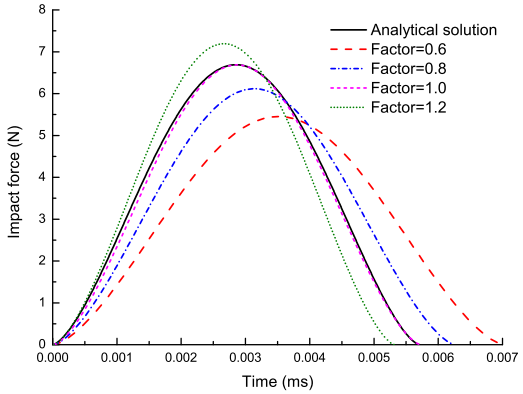

Figure 6: Comparison of the time histories of the contact force with different penalty factors - Hertz contact model

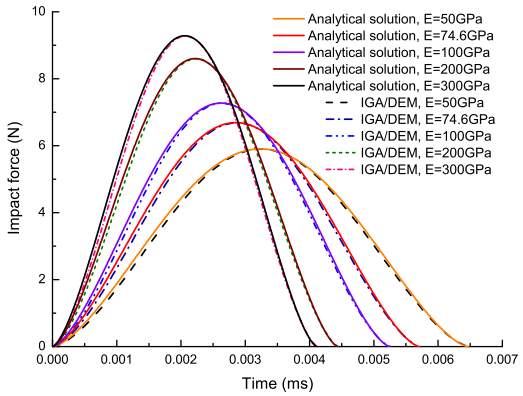

Figure 7: Comparison of the time histories of the contact force with different Young's moduli of the impact ball - Hertz contact model ($\lambda = 1.0$)

The results show that the numerical results with $\lambda = 1.0$ are in good agreement with the analytical solutions. The figure also demonstrates that the Young's modulus of the discrete sphere has great effects on the contact force between a DE and an IG element. It is clear from Eqs. (23) and (32) that the contact model with a larger Young's modulus of DE will result in a higher peak value of the force and a shorter impact duration.

The contact-force histories of the impact ball with Poisson's ratios ν= 0.1, 0.2285, 0.3 and 0.4 and the penalty factor $\lambda = 1.0$ are compared with the analytical solutions and shown in Fig. 8. The numerical results agree very well with the analytical solutions. This figure also shows that the Poisson's ratio of DE has relatively minor effects on the IGA/DEM contact force, although a smaller Poisson's ratio tends to results in a lower peak value and a longer duration of the contact-force curve.

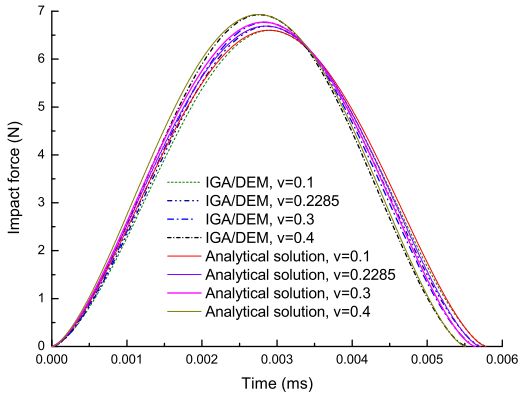

Figure 8: Comparison of the time histories of the contact force with different Poisson's ratios of the impact ball - Hertz contact model ($\lambda = 1.0$)

5.2. Linear and quadratic contact models

Both linear and quadratic models are considered next. The contact force histories computed from the two models with different penalty factors λ are shown in Figs. 9 and 10 respectively. Note that the values of λ are specially selected so that the resulting contact forces are close to the analytical solution.

Fig. 9 clearly demonstrates that the penalty factor λ has a significant effect on the contact force. In general, the linear contact model has a steeper slope than the analytical one at the beginning and ending of the contact.

When the penalty factor is specially chosen such that the linear model obtains the same impact duration as the analytical solution, the corresponding peak value is lower than the true value. On the other hand, when the linear model with $\lambda = 0.055$ reaches the same peak value as the analytical one, the corresponding contact duration is much shorter. In other words, the results demonstrate that the peak and duration calculated from the linear model can hardly agree with the analytical ones simultaneously. Thus, it is concluded that the linear penalty function model seems not suitable for the contact force calculations between DEM and IGA.

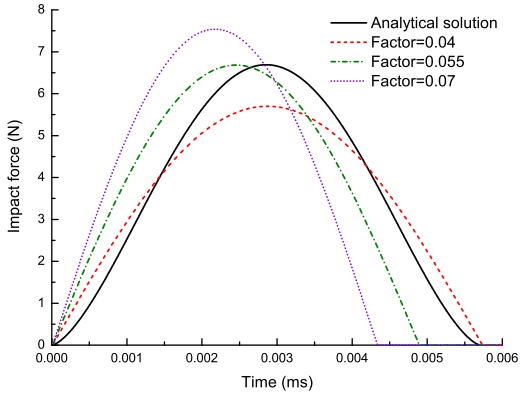

Figure 9: Comparison of the time histories of the contact force calculated from linear penalty function with different penalty factors - the linear contact model

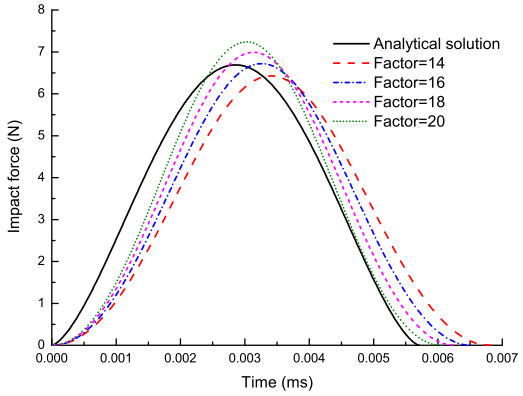

Figure 10: Comparison of the time histories of the contact force calculated from quadratic penalty function with different penalty factors - the quadratic contact model

For the quadratic model as shown in Fig. 10, the slope of its contact-force curves is much gentler than the analytical one at the beginning and ending of the contact. The peak value and impact duration of the quadratic model cannot match those of the analytical ones at the same time. Again, it is clear that the quadratic contact model seems not suitable for the contact force calculations between DEM and IGA.

Finally, the contact-force histories from the three contact models are shown in Fig. 11 and compared with the analytical solution. In this figure, the penalty factor λ used for each contact model considered is chosen to result in the same peak force value as the analytical one. It is concluded that only the Hertz contact model with the penalty factor $\lambda = 1.0$ can achieve a very good agreement with the analytical result for the benchmark example.

Note that the plate in this example is fairly thick to make the analytical solution valid. It is not clear, however, that the Hertz contact model will still be equally applicable for thin plates. In this case, the impact duration may be comparably larger than the travel time of the stress wave before reflecting during the impact. Possible multiple reflection of the stress wave along the thickness of the plate makes it difficult to derive an analytical solution that can be employed to further assess the suitability of various contact models for the coupled modelling of both discrete elements and IGA elements. Further work is therefore worth being pursued.

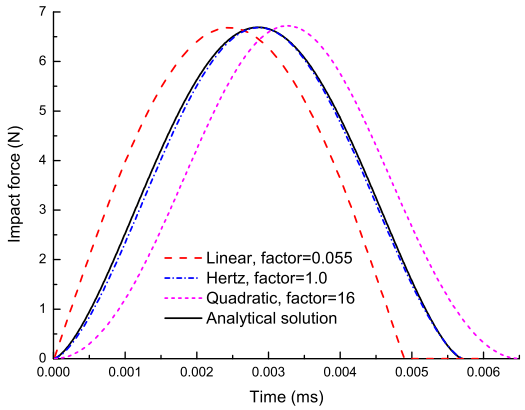

Figure 11: Comparison of the time histories of the contact force calculated from the three models with the analytical solution

6. Illustrative example

In order to demonstrate the applicability and robustness of the proposed coupling method, one illustrative example involving contacts between DEs and deformable NURBS surfaces is simulated. The example involves granular particle materials impacting a tailor rolled blank (TRB) plate. The dimensions and other geometric details of the plate are shown in Fig. 6.

3488 spherical particles with radii ranging from 0.4 to 0.6 mm are first randomly packed in a cylindrical domain above the TRB. There is about 0.1 mm gap between the lowest particles and the top control nodes of the TRB in the central region. The particles are released with an initial velocity of 10.0 m/s to impact the plate.

The material properties of the particles and the TRB are listed in Table 3. The particles are modeled as spherical discrete elements and the TRB is modeled by 1332 second-degree solid elements of IGA. The Hertz contact model without the penalty factor correction is applied to account for both DE/DE and DE/IGA contact interactions. The time step used in the central difference scheme for the time integration of the dynamic system is set to be 10^{-5} ms which is smaller than the required critical time step .

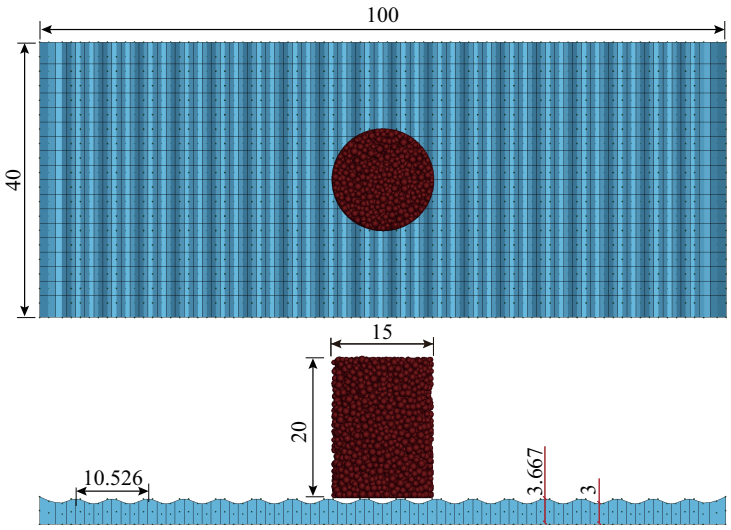

Figure 12: The dimensions of granular particles impacting a TRB system (unit: mm)

Both the total impact force acting on the TRB and the displacement in the vertical direction at the center of the TRB bottom surface are displayed

Table 3: Radius, initial velocity of particles, and material properties of particles and TRB

Initial velocity of particles, V	10.0 m/s
Particle radius, r	$0.4 \sim 0.6$ mm
Mass density of particles and TRB, ρ	10^{-2} g/mm^3
Young's modulus of particles and TRB, E	1.0 GPa
Poisson's ratio of particles and TRB, ν	0.0

against time in Fig. 13. The impact force initially increases from the beginning to about 0.2 ms, then fluctuates and finally decreases. In the time interval [0.2, 1.0]ms, the impact force still fluctuates but remains relatively small. From 0 ms to 1.0 ms, the displacement increases because most particles maintain in contact with the TRB instead of bouncing back.

The configurations of the particles and the velocity distributions are displayed in Fig. 14 at six different time instants. As the particles move downwards, some lower particles are in contact with the crest area of the top surface of the TRB first and the velocities of these particles begin to decrease as shown in Fig. 14(a). Then more particles come into contact with the TRB top surface as shown in Fig. 14(b). Afterwards, the particles scatter around because of the uneven TRB top surface and random initial arrangement of particles, as shown in Figs. 14(c) and (d). Subsequently, more particles scatter in a larger area and are in contact with the top surface of the TRB (see Fig. 14(e)-(f)). In the whole impact process, no large penetration is observed between the particles and the TRB.

7. Conclusions

A three-dimensional coupled isogeometric/discrete-element method has been developed to take the advantages of the geometry smoothness in isogeometric analysis and the effective handling of particle contacts in discrete element modelling. In the coupling phase, candidate contact pairs are detected by modifying the CGRID method, and the exact contact position between a spherical discrete element and a NURBS surface is obtained by modifying the simplex and Brent iterations in the local search/resolution. To calculate the contact force between a DE and an IGA element accurately, several contact models, including linear, Hertz and quadratic models with penalty factor correction, have been investigated. Based on the simulation of a benchmark problem - a ball impacting a thick plate, it is found that

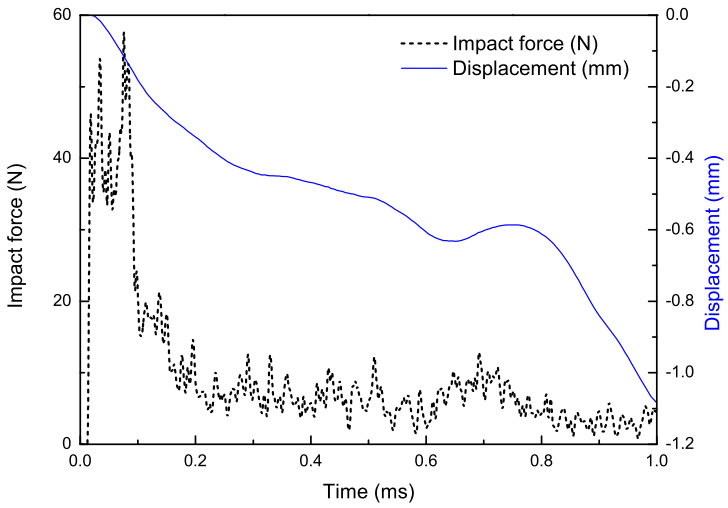

Figure 13: The impact force and displacement history of TRB

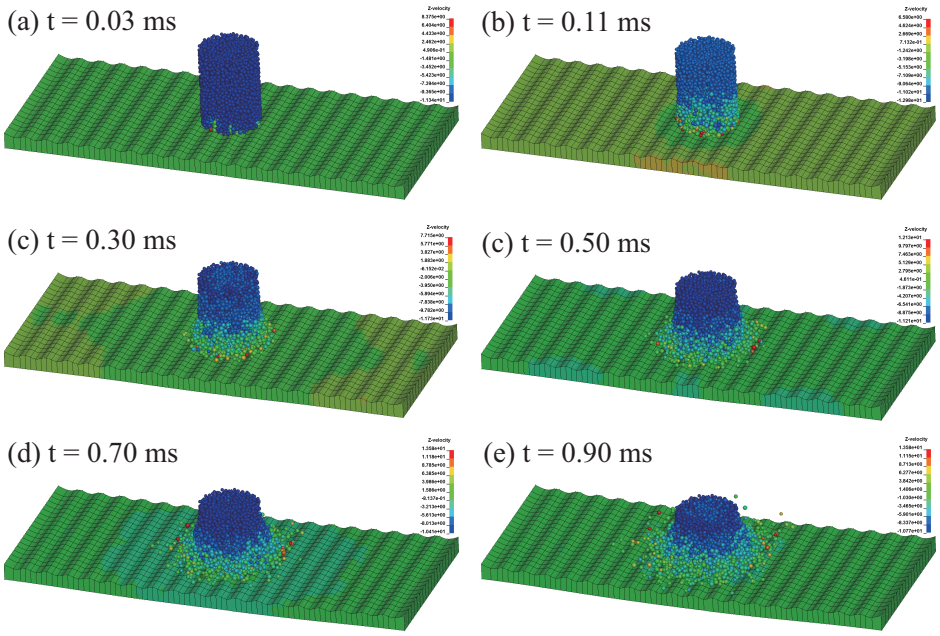

Figure 14: The velocity distributions in the vertical direction and the particle configurations at six time instants: (a) t = 0.03 ms, (b) t = 0.11 ms, (c) t = 0.3 ms, (d) t = 0.5 ms, (e) t = 0.7 ms, (f) t = 0.9 ms

the Hertz contact model agrees very well with the analytical solution, and no penalty factor correction is needed. The applicability and robustness of the coupling approach has also been demonstrated through the simulation of an example involving random arranged granular particles impacting a tailor rolled blank in the elastic regime.

It is noted, however, that it is not clear if the Hertz contact model will still be accurate for thin plate cases. Furthermore, more work needs to be done to establish what contact models should be adopted when elasto-plastic deformation of the structure needs to be considered.

Acknowledgment

This work is supported by NNSF of China (Grant Nos. 51878184 and 51404209). The support is greatly acknowledged.

Compliance with ethical standards

Conflicts of interest The authors declare that they have no conflict of interest.

References

[1] Cundall PA, Strack OD. A discrete numerical model for granular assemblies. Geotechnique 1979;29(1):47–65.

[2] Munjiza AA, Knight EE, Rougier E. Computational mechanics of discontinua. John Wiley & Sons; 2011.

[3] Gao W, Liu L, Liao Z, Chen S, Zang M, Tan Y. Discrete element analysis of the particle mixing performance in a ribbon mixer with a double u-shaped vessel. Granular Matter 2019;21(1):12. doi:10.1007/s10035-018-0864-4.

[4] Han K, Peric D, Owen D, Yu J. A combined finite/discrete element simulation of shot peening processes–part II: 3D interaction laws. Engineering Computations 2000;17(6):680–702.

[5] Munjiza AA. The combined finite-discrete element method. John Wiley & Sons, England; 2004.

[6] Owen D, Feng Y, de Souza Neto E, Cottrell M, Wang F, Andrade Pires F, et al. The modelling of multi-fracturing solids and particulate media. International Journal for Numerical Methods in Engineering 2004;60(1):317–39.

[7] Onate E, Rojek J. Combination of discrete element and finite element methods for dynamic analysis of geomechanics problems. Computer methods in applied mechanics and engineering 2004;193(27-29):3087–128.

[8] Xiang J, Munjiza A, Latham JP. Finite strain, finite rotation quadratic tetrahedral element for the combined finite–discrete element method. International journal for numerical methods in engineering 2009;79(8):946–78.

[9] Zang M, Gao W, Lei Z. A contact algorithm for 3D discrete and finite element contact problems based on penalty function method. Computational Mechanics 2011;48(5):541–50.

[10] Gao W, Tan Y, Jiang S, Zhang G, Zang M. A virtual-surface contact algorithm for the interaction between FE and spherical DE. Finite Elements in Analysis and Design 2016;108:32–40.

[11] Zheng Z, Zang M, Chen S, Zeng H. A GPU-based DEM-FEM computational framework for tire-sand interaction simulations. Computers & Structures 2018;209:74–92.

[12] Munjiza A, Knight EE, Rougier E. Large strain finite element method: a practical course. John Wiley & Sons; 2015.

[13] Dang HK, Meguid MA. An efficient finite-discrete element method for quasi-static nonlinear soil-structure interaction problems. International Journal for Numerical and Analytical Methods in Geomechanics 2013;37(2):130–49.

[14] Tran V, Meguid M, Chouinard L. A finite-discrete element framework for the 3D modeling of geogrid-soil interaction under pullout loading conditions. Geotextiles and Geomembranes 2013;37:1–9.

[15] Hu L, Hu G, Fang Z, Zhang Y. A new algorithm for contact detection between spherical particle and triangulated mesh boundary in discrete

element method simulations. International Journal for Numerical Methods in Engineering 2013;94(8):787–804.

[16] Chen H, Zhang Y, Zang M, Hazell PJ. An accurate and robust contact detection algorithm for particle-solid interaction in combined finite-discrete element analysis. International Journal for Numerical Methods in Engineering 2015;103(8):598–624.

[17] Gao W, Zang M. The simulation of laminated glass beam impact problem by developing fracture model of spherical DEM. Engineering Analysis with Boundary Elements 2014;42:2–7.

[18] Wriggers P. Computational contact mechanics, 2nd edn. Springer-Verlag, Berlin; 2006.

[19] Santasusana M. Numerical techniques for non-linear analysis of structures combining discrete element and finite element methods. Ph.D. thesis; Polytechnic University of Catalonia; 2017.

[20] Feng Y, Owen D. A 2D polygon/polygon contact model: algorithmic aspects. Engineering Computations 2004;21(2/3/4):265–77.

[21] Feng YT, Han K, Owen DRJ. Energy-conserving contact interaction models for arbitrarily shaped discrete elements. Computer Methods in Applied Mechanics and Engineering 2012;205-208:169–77.

[22] Hughes TJ, Cottrell JA, Bazilevs Y. Isogeometric analysis: CAD, finite elements, NURBS, exact geometry and mesh refinement. Computer Methods in Applied Mechanics and Engineering 2005;194(39-41):4135–95.

[23] Cottrell JA, Hughes TJ, Bazilevs Y. Isogeometric analysis: toward integration of CAD and FEA. John Wiley & Sons; 2009.

[24] Gao W, Wang J, Yin S, Feng Y. A coupled 3D isogeometric and discrete element approach for modelling interactions between structures and granular matters. Computer Methods in Applied Mechanics and Engineering 2019;354:441–63.

[25] Cox MG. The numerical evaluation of b-splines. IMA Journal of Applied Mathematics 1972;10(2):134–49.

[26] De Boor C. On calculating with b-splines. Journal of Approximation theory 1972;6(1):50–62.

[27] Temizer I, Wriggers P, Hughes T. Contact treatment in isogeometric analysis with NURBS. Computer Methods in Applied Mechanics and Engineering 2011;200(9-12):1100–12.

[28] Di Renzo A, Di Maio FP. Comparison of contact-force models for the simulation of collisions in DEM-based granular flow codes. Chemical Engineering Science 2004;59(3):525–41.

[29] Escotet-Espinoza MS, Foster CJ, Ierapetritou M. Discrete element modeling (DEM) for mixing of cohesive solids in rotating cylinders. Powder Technology 2018;335:124–36.

[30] Johnson KL, Johnson KL. Contact mechanics. Cambridge University Press; 1987.

[31] Williams JR, Perkins E, Cook B. A contact algorithm for partitioning n arbitrary sized objects. Engineering Computations 2004;21(2/3/4):235–48.

[32] De Lorenzis L, Wriggers P, Zavarise G. A mortar formulation for 3d large deformation contact using NURBS-based isogeometric analysis and the augmented Lagrangian method. Computational Mechanics 2012;49(1):1–20.

[33] Kim JY, Youn SK. Isogeometric contact analysis using mortar method. International Journal for Numerical Methods in Engineering 2012;89(12):1559–81.

[34] De Lorenzis L, Wriggers P, Hughes TJ. Isogeometric contact: a review. GAMM-Mitteilungen 2014;37(1):85–123.

[35] De Lorenzis L, Temizer I, Wriggers P, Zavarise G. A large deformation frictional contact formulation using NURBS-based isogeometric analysis. International Journal for Numerical Methods in Engineering 2011;87(13):1278–300.

[36] Dimitri R, De Lorenzis L, Scott M, Wriggers P, Taylor R, Zavarise G. Isogeometric large deformation frictionless contact using T-splines.

Computer methods in applied mechanics and engineering 2014;269:394–414.

[37] Matzen M, Cichosz T, Bischoff M. A point to segment contact formulation for isogeometric, NURBS based finite elements. Computer Methods in Applied Mechanics and Engineering 2013;255:27–39.

[38] Moré JJ, Cosnard MY. Numerical solution of nonlinear equations. ACM Transactions on Mathematical Software (TOMS) 1979;5(1):64–85.

[39] Brent RP. Some efficient algorithms for solving systems of nonlinear equations. SIAM Journal on Numerical Analysis 1973;10(2):327–44.

[40] Kopaka J, Gabriel D, Pleek J, Ulbin M. Assessment of methods for computing the closest point projection, penetration, and gap functions in contact searching problems. International Journal for Numerical Methods in Engineering 2016;105(11):803–33.

[41] Spendley W, Hext GR, Himsworth FR. Sequential application of simplex designs in optimisation and evolutionary operation. Technometrics 1962;4(4):441–61.

[42] Zheng Z, Zang M, Chen S, Zhao C. An improved 3D DEM-FEM contact detection algorithm for the interaction simulations between particles and structures. Powder Technology 2017;305:308–22.

[43] Reed J. Energy losses due to elastic wave propagation during an elastic impact. Journal of Physics D: Applied Physics 1985;18(12):2329.

[44] McLaskey GC, Glaser SD. Hertzian impact: Experimental study of the force pulse and resulting stress waves. The Journal of the Acoustical Society of America 2010;128(3):1087–96.